An aerostatic pad compensated by a differential diaphragm valve

Tribology International 191 (2024) 109103

Contents lists available at ScienceDirect

Tribology International

journal homepage: www.elsevier.com/locate/triboint

An aerostatic pad compensated by a differential diaphragm valve

Federico Colombo, Luigi Lentini *, Andrea Trivella, Terenziano Raparelli

Department of Mechanical and Aerospace Engineering, Politecnico di Torino, Corso Duca degli Abruzzi 24, Turin 10129, Piedmont, Italy

ARTICLE INFO

Keywords:
Aerostatic pad
Infinite stiffness
Compensation method
Diaphragm valve

ABSTRACT

This paper presents a novel prototype of a passively compensated aerostatic pad which consists in the integration of a commercial pad with a custom-built differential diaphragm valve. The static performance of the system is experimentally assessed in the presence of different supply and reference pressures. Additionally, the paper describes two lumped parameter models of the system which present different level of complexity. Experimental and numerical results are in good agreement and demonstrate that the static performance of the system can be computed more quickly through the simplified version of the described models.

1. Introduction

Due to their zero friction and minimal environmental impact, aerostatic bearings align well with the sustainability objectives outlined in the European Green Deal [1]. Bibliometric evidence reveals a growing research interest in air bearing technology [2]. Despite their relatively low stiffness and limited damping characteristics, air bearings have remained indispensable components in numerous applications, including precision measuring instruments, positioning machinery, inertial navigation systems, and ultra-precision machine tools [3,4].

Since the mid-20th century, the primary focus of gas bearing research has been to overcome the limitations associated with lubricant compressibility. The aim has been to enhance load capacity and stiffness while preserving dynamic stability [5,6]. Various approaches have been proposed in pursuit of this goal. Classical engineering methods have centered on improving static performance, often relying on dimensionless charts derived from closed-form solutions [7,8] or semi-empirical formulations [9]. With the advent of powerful electronic calculators, researchers have been able to develop highly accurate numerical models for simulating and optimizing both static and dynamic performance in conventional aerostatic bearings, including orifice-type, grooved, and porous bearings. These optimizations have been achieved through sensitivity analysis [10,11] and even artificial neural networks [12]. Additionally, studies have been conducted to mitigate the impact of vortex-induced vibrations and nano-level vibrations [13]. However, these analytical, empirical and numerical approaches lead to limited enhancements of the overall performance [14,15].

In contrast, passive and active compensation methods have proven to be more effective in achieving bearings with superior performance [16]. These methods consist in enhancing the bearing performance through the integration of pads with additional elements or devices. Passive compensation methods use components which require only the energy associated with the supply pressure of the bearing, e.g., pneumatic valves and compliant elements. By contrast, actively compensated bearings are equipped with elements such as sensors, controllers and actuators that require external sources of energy to function. The presence of closed-loop systems in active compensation methods allows for substantial improvements in both static and dynamic performance. Closed control loops can be used to adapt the mechanical structure of the system [17–21] or to regulate the air flow supplied to the air gap [22–24]. Despite their superior performance, active compensation solutions remain cost-prohibitive for most industrial applications. In contrast, passive compensation methods offer a cost-effective alternative, albeit with limited bandwidth. Passive compensation methods usually exploit the compliance of elastic elements or pneumatic valves to improve bearing behaviours. Blondeel et al. [25,26], Snoeys and Al-Bender [27], Holster and Jacobs [28] and Bryant et al. [29] proposed passively compensated bearings with convergent gap geometry. These solutions consist in the use of compliant surface to suitably modify the air gap pressure distribution in the presence of load variations. The use of movable or elastic orifices are among the more adopted passive compensation strategies. Yoshimoto et al. [30] designed an aerostatic thrust bearing with a self-controlled restrictor. It consists in the integration of a floating disk inside the supply system of the bearing. This solution exploits the pressure acting on the two sides of the floating disk to control the air flow supplying the air gap. Results demonstrate that by

* Corresponding author.
E-mail address: luigi.lentini@polito.it (L. Lentini).

https://doi.org/10.1016/j.triboint.2023.109103
Received 4 October 2023; Received in revised form 6 November 2023; Accepted 10 November 2023
Available online 14 November 2023

using this method bearings may exhibit a level of static stiffness ten times higher than conventional aerostatic thrust bearings. Similar results were obtained by Newgard et al. [31] who proposed the use of elastic orifices to improve air pad performance. Kodnyanko et al. [32,33] proposed and investigated the performance of an aerostatic bearing in which decrease in compliance is ensured by the use of air throttling with elastic orifices. Chen and Lin [34,35] proposed a disk-spring compensator to increase the static and dynamic performance bearing. Wu et al. [36] studied the effect of introducing pressure equalizing groove. Ghodsiyeh et al. [10,11] experienced the use of a custom-built diaphragm valve to increase air pad stiffness. In the presence of load variations, the valve makes it possible to increase the stiffness by a suitable regulation of the air supplied to the pad. Furthermore, in [10,11], a numerical procedure was presented for the appropriate design of valve parameters, taking into consideration the chosen working air gap height [37].

This paper describes a novel prototype of passively compensated aerostatic pad. Differently from previous solutions [38], this compensation solution employs a differential diaphragm valve that presents a fixed nozzle and a moving shutter that regulates the inflow supplied to the controlled air pad. Thanks to the presence of four chambers the relative distance between the nozzle and the shutter depends on a feedback pressure taken from the air gap and a reference pressure which may be appropriately defined by users.

2. Materials and methods

2.1. The proposed prototype

The proposed prototype is a passively compensated system that consists in the integration of an air pad and a custom-built differential diaphragm valve. Fig. 1a shows a photograph of the prototype.

As shown in Fig. 1b, the air pad presents a rectangular base whose dimensions are L= 110 mm and B= 50 mm. The air flow supplied to the clearance is provided by means of four supply holes located in the middle of each side of a grooved rectangular supply line whose dimensions are l= 80 mm and b= 30 mm. The grooves present a triangular cross-section with a base of w_g= 0.3 mm and a height of h_g= 0.06 mm. The active surface of the pad also presents a pressure intake to measure the air gap pressure. The diameter of the pressure intake and the supply holes of the pad was verified via an electronic microscope. Fig. 2 shows some of the geometrical data acquired during these experiments.

The supply holes and the pressure intakes are pocketed orifices. The supply holes have a nominal diameter d_p= 0.5 mm and they feed trapezoidal pockets where the larger nominal diameter is D_p= 0.8 mm. The pressure intake has a nominal diameter d_{fb}= 0.25 mm and a cylindrical pocket with a nominal diameter of D_{fb}= 0.5 mm. Fig. 3 shows a photo (Fig. 3a) and a scheme (Fig. 3b) of the custom-built differential diaphragm valve.

The valve presents four chambers that are sealed and separated by three rubber membranes. At the outer edges, the membranes are secured between the four primary components that make up the valve (part 1, 2, 3 and 4), while at their central section, they are attached to a mobile shutter. Chambers 1 and 4 are supplied with the same constant pressure P_s by means of a pressure reducer. Chamber 2 is supplied by the air gap feedback pressure P_{fb} through the pressure intake drilled on the air pad surface. Chamber 3 is supplied with a constant reference pressure P_{rif}. As the pressures in chambers 1 and 4 remain equal, the equilibrium position of the moving shutter is determined by the pressure values within chambers 2 and 3. Once integrated, the valve supplies compressed air to the pad via a nozzle that is fixed on the upper part of the valve (part 1). To avoid the presence of air leakages, the body of the nozzle is sealed by two o-rings. The amount of air flow provided to the pad depends on the distance between the nozzle and shutter. Fig. 4 shows a functional scheme to illustrate the working principle of the system.

Under steady-state working conditions, the system is loaded via an external force F that corresponds to a static air gap height h and air consumption G=G_1=G_2=G_3. In a conventional commercial pad, an

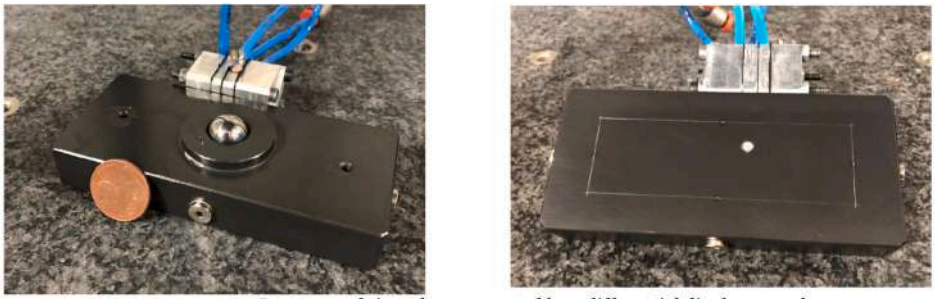

a: Prototype of air pad compensated by a differential diaphragm valve.

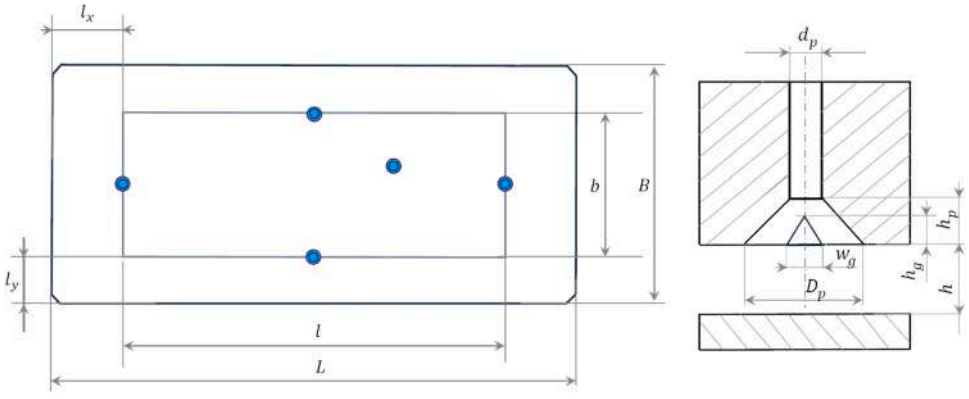

b: Aerostatic pad geometry.

Fig. 1. a: Prototype of air pad compensated by a differential diaphragm valve. b: Aerostatic pad geometry.

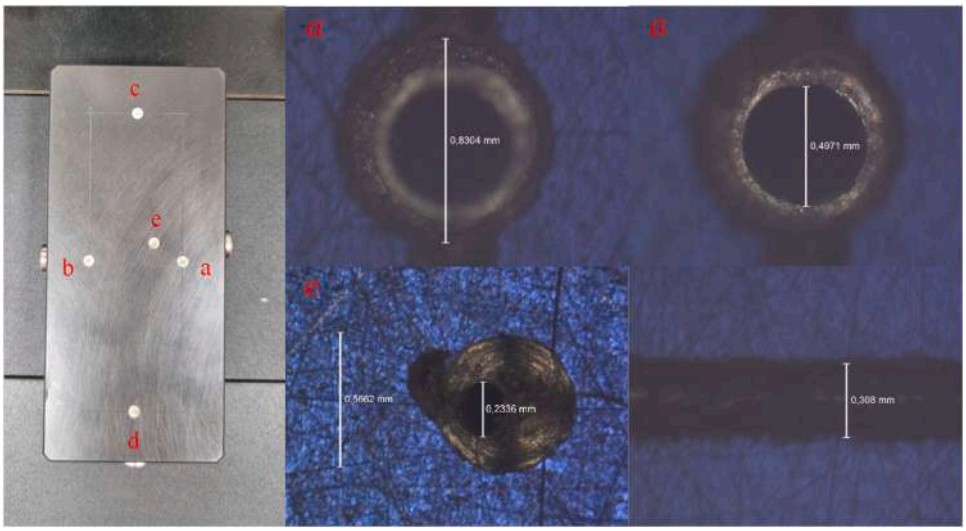

Fig. 2. Geometry of the air pad feeding system.

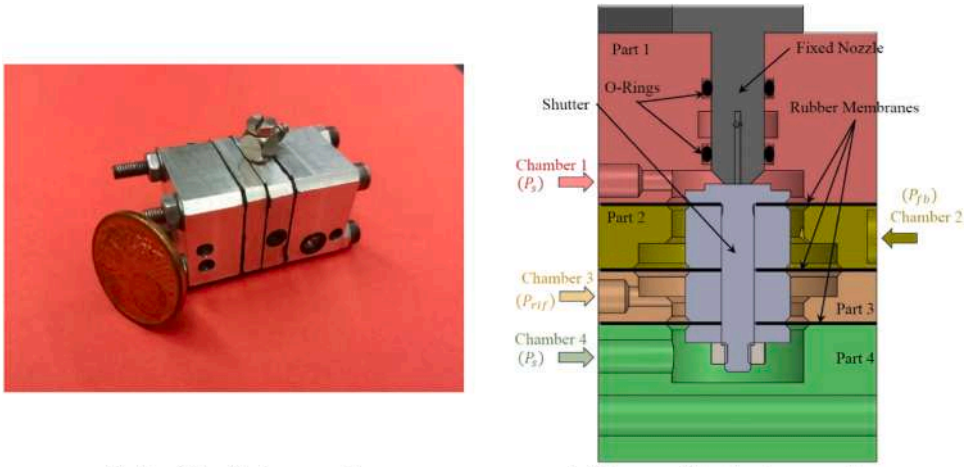

Fig. 3. The custom-built differential diaphragm valve.

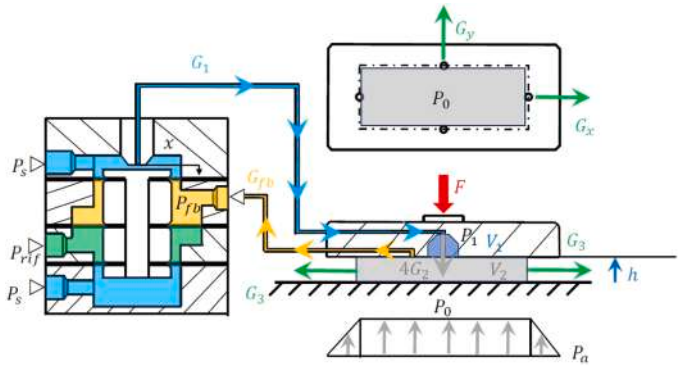

Fig. 4. Working principle of the system.

external load increase (decrease) would generate a reduction (increase) of the air gap height $h - \Delta h$ and in turn a reduction (increase) of the air mass flow rate exhausted from it $G_3 - \Delta G_3$ ($G_3 + \Delta G_3$). Conversely, the proposed prototype makes it possible to compensate for load variations by restoring the initial air gap height h, i.e., the system exhibits quasi-static infinite stiffness. In this case, the load increase ΔF generates an increase (decrease) of the mean air gap pressure P_0 and in turn an increase (decrease) of the feedback pressure P_{fb}. Subsequently, the feedback pressure variation produces a downward motion of the shutter thus increasing (decreasing) its distance from the fixed nozzle of Δx. The increment (reduction) of the shutter-nozzle distance increases (decreases) the conductance of the air pad feeding system thus increasing the inflow into the air gap ΔG_2 till the mean pressure P_0 reaches a suitable value to restore the initial air gap height h.

2.2. The adopted test bench

Fig. 5 shows a photo (Fig. 5a) and a scheme (Fig. 5b) of test bench adopted in this study.

The mechanical structure of the test bench consists of a loading chain that can impose static or dynamic force upon the pad under test. Starting from the upper part, the loading chain consists of a shaker, a stinger, a pneumatic cylinder, a load cell and a spherical loading tip. The shaker and the stinger make it possible to superimpose dynamical forces to the static ones generates by the pneumatic cylinder. The load cell is interposed between the pneumatic cylinder and the loading tip to measure the force applied to the pad. The air gap height of the pad is indirectly measured from the pad displacement. The motion of the pad is measured by four capacitive sensors that are fixed on a sensor carrier at the corners

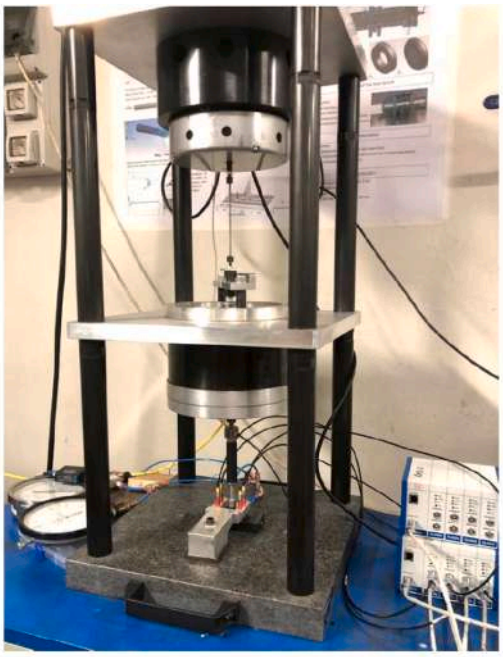

a: Photo of the test bench

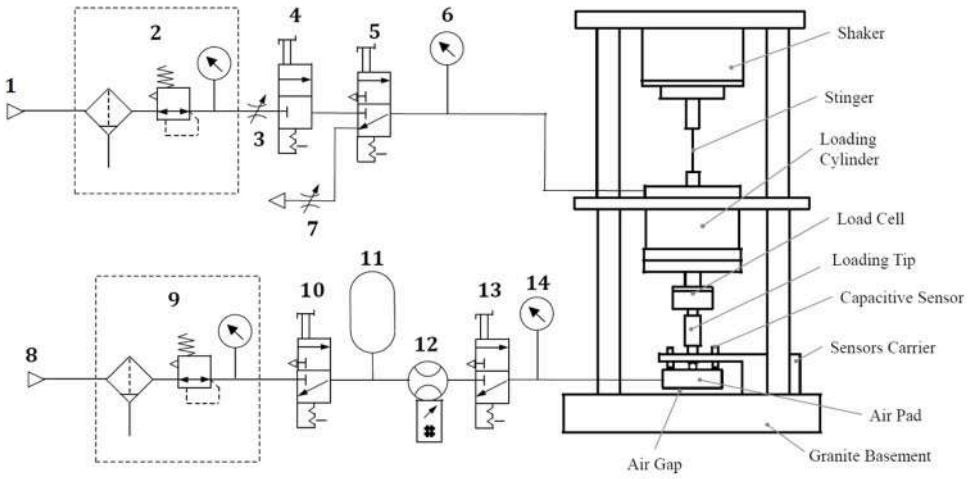

b: Scheme of the test bench.

Fig. 5. test bench photo and scheme.

of a 35 × 20 mm^2 rectangle that is centred with respect to the pad. The test bench also presents two feeding lines. The first one (in the upper part of Fig. 5b) makes it possible to vary the static force applied upon the pad by charging or discharging the chamber inside the loading cylinder. It consists of a pressure source (1), Filter Reducer Lubricator (FRL) system (2), two variable resistances (3 and 7), a 2/2-ways valve (4), a 3/2-ways valve (5) and a manometer (6). Here, the FRL system guarantees the absence of contaminants, e.g., dust and oil particles in the supplied air. When the pneumatic valves 4 and 5 are manually switched, the pressure inside the chamber of the cylinder increases and its time rate can be defined acting on the variable resistance (3). Conversely, the pressure inside the cylinder can be reduced when the feeding line is in the configuration indicated in Fig. 5b. The second feeding line (in lower part of Fig. 5b) supplies compressed air to the pad prototype and consists of a pressure source (8), a FRL system (9), two 3/2-ways pneumatic valves (10 and 13), an air tank (11), a digital flowmeter (12) and a manometer (14). Here, switching the pneumatic valve (10) makes it possible to fill the supply tank (11). The presence of this supply tank is used to stabilize the pressure upstream of the pad. The pneumatic valve (13) makes it possible to connect the feeding tank with the pad under test. The flowmeter (12) and the manometer (14) are used to measure the air consumption and the supply pressure of the pad.

2.3. Experimental Procedure

The performance and the functioning of the proposed prototype were verified by means of static tests performed through the test bench described in Section 2.2. The load capacity and air consumption curve of the protype were obtained by performing the following experimental procedure:

1. The pad under investigation was located on the test rig.
2. An initial preload was applied on the pad by varying the length of the loading tip.

3. Valves 10 and 13 were switched to provide supply air to the pad under test.
4. Once the variable resistances 3 and 7 were suitably set, valves 5 and 4 were switched to gradually increase the static load applied on the pad.
5. Once the maximum value of external force was reached, valve 4 was switched to keep the external force constant.
6. Valves 13 and 5 were switched to cut off the air supplied to the pad and to reduce the pressure within the pneumatic cylinder, i.e., the external load.
7. The test continued until the external force reached the value of the initial preload.
8. End of the test

It should be noted that the time rate of the force applied on the pad has to be sufficiently small, given that this is a static characterization procedure. Fig. 6 shows an example of the curves that were obtained by recording the data related to the load cell, the capacitive sensors and the flowmeter between the step 4 and 6 of the described procedure.

Figs. 6a and 6b shows the load capacity and the air consumption curve before the process of data elaboration. These graphs are supplemented with numbers related to the adopted procedure. The four capacitive sensors (x_1, x_2, x_3, x_4) make it possible to measure the pad displacement and assess the presence of tilting motion that may be caused by incorrect positioning or malfunctions. Once the test is successfully completed, the mean displacement of the pad is computed from the capacitive sensors and the air gap height is obtained from the rough load capacity curve by subtracting the curve Section 7 from the curve Section 4.

3. Lumped parameter models

The proposed compensated pad was modelled through lumped parameter models consisting of pneumatic resistances and capacitances. The present section describes two version of the lumped parameter model of the system: a complete and a simplified version. The simplified model considers solely the dynamic equations related to air gap and the pad (see Eqs. 8, 9 and 10). The complete model also considers the dynamics of the shutter and the volume of the feedback chamber (see Eqs. 2, 8, 9, 10 and 11). The models were implemented in Matlab and their dynamic equations were discretised by the finite difference method and integrated using the Forward Euler scheme. The structure of the models resembles those described in [39,40]. Figs. 4, 7, and 8 can be useful to better interpret the physics related to the model and the implemented prototype. The following sections (Sections 3.1, 3.2 and 3.3) provide the equations of the two lumped parameter models and the structure of the implemented algorithm.

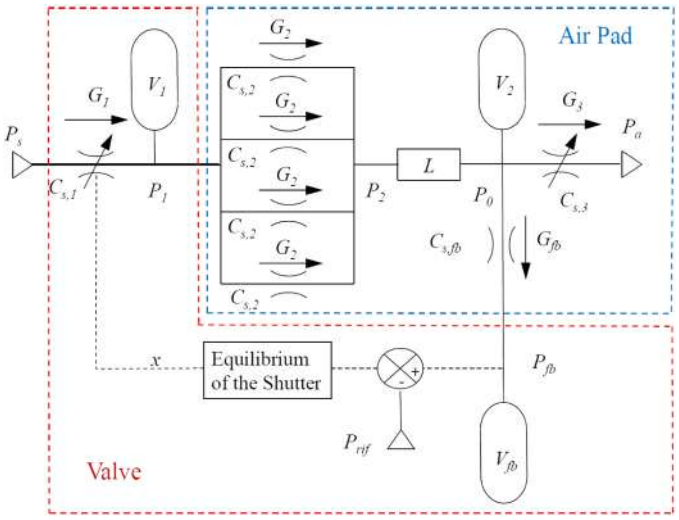

Fig. 7. Pneumatic scheme of the complete model.

3.1. Complete model

Fig. 7 shows the pneumatic scheme of the complete model of the system.

Here, the valve is supplied with pressurised air at the pressure P_s. The air mass flow rate G_1 passing through the nozzle of the valve is computed by means of a mathematical formulation similar to that described in ISO 6358 [41,42]:

$$G_1 = K_T C_{s,1} P_s \sqrt{1 - \left(\frac{\frac{P_1}{P_s} - b_c}{1 - b_c}\right)^2} \tag{1}$$

$$K_T = \sqrt{\frac{293}{T}} \tag{1a}$$

$$C_{s,1} = 1.05\left(1 - 0.3e^{-0.005\mathrm{Re}_1}\right) \frac{0.685}{\sqrt{R_g T}} \pi x d_n \tag{1b}$$

$$\mathrm{Re}_1 = \frac{G_1}{\pi \mu d_n} \tag{1c}$$

where, R_g and T are the specific heat ratio and temperature of the supplied air, b_c is the theoretical critical pressure ratio (0.5283), P_1 is the absolute pressure inside the body of the pad, $C_{s,1}$ and d_n are the

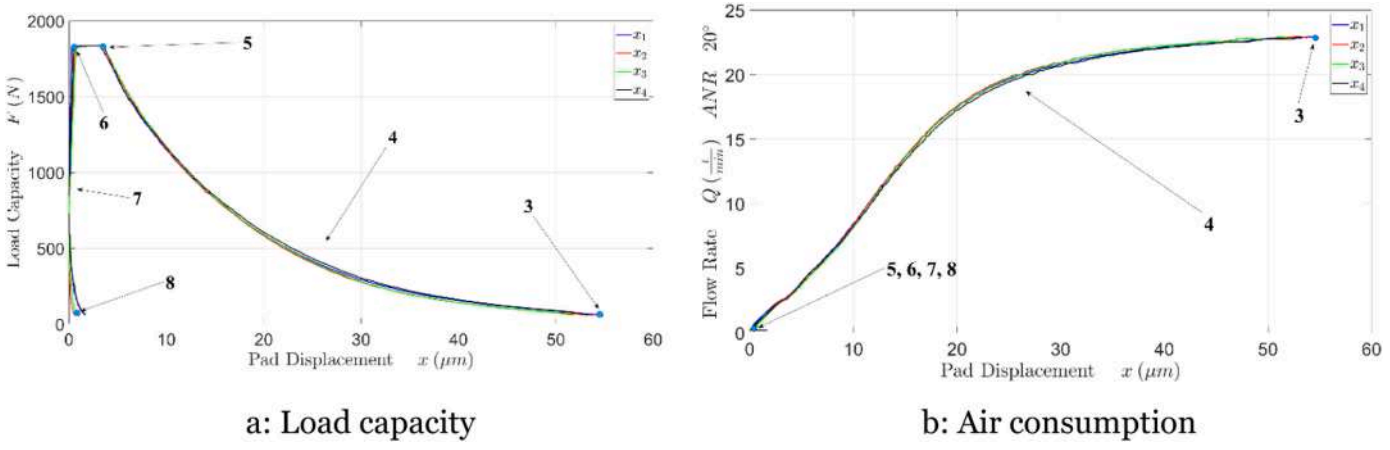

Fig. 6. Curves obtained through the described static experimental procedure.

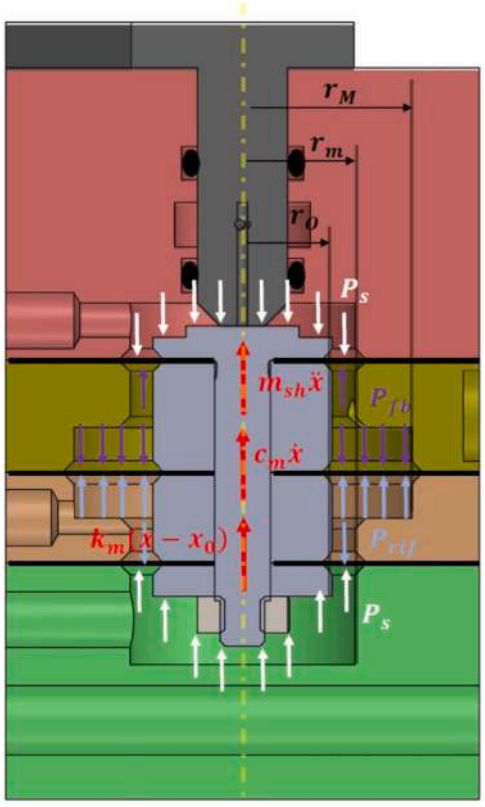

Fig. 8. Free body diagram of the shutter.

conductance and diameter of the valve nozzle and Re_1 is the Reynolds number related to the air mass flow rate G_1. x is the distance between the nozzle and the shutter of the valve and it is computed on through the equilibrium equation of the shutter (Eq. 2).

$$m_{sh}\ddot{x} + c_m\dot{x} + k_m x = \frac{\pi\left(d_M^2 - d_m^2\right)}{4}\left(P_{fb} - P_{rif}\right) \tag{2}$$

Where,x, $\dot{x}$, $\ddot{x}$, $r_0 = d_0/2$ and m_{sh} are the displacement, velocity, acceleration, radius and mass of the shutter, while x_0 is its initial distance from the nozzle. c_m and k_m are the damping and stiffness coefficients related to the rubber membrane. $d_M = 2r_M$ and $d_m = 2r_m$ are the diameter of chambers 1–4 and 2–3. The mass of the shutter m_{sh} was taken equal to the real mass (2.35 g), whereas the equivalent stiffness k_m and damping c_m of the membrane were numerically identified depending on the operating condition imposed during the experiments. Eq. 2 can be easily obtained from the scheme reported in Fig. 8.

The air mass flow rate G_1 supplies the volume of the pad chamber V_1 whose absolute pressure is indicated as P_1. Before reaching the air gap volume V_0, compressed air passes through the supply orifices of the pad. It is worth pointing out that the volume downstream of the supply holes V_2 is the sum of the air gap $V_0 = lbh$ and the grooves volumes $V_g = 2w_g h_g(l+b)$ (see Eq. 10a). This air flow is indicated as G_2 and is computed through Eq. 3.

$$G_2 = K_T C_{s,2} P_1 \sqrt{1 - \left(\frac{\frac{P_2}{P_1} - b_c}{1 - b_c}\right)^2} \tag{3}$$

$$C_{s,2} = 1.05\left(1 - 0.3e^{-0.005\mathrm{Re}_2}\right) \quad \frac{0.685}{\sqrt{R_g\ T}} \quad \left(\pi \quad d_p \quad h + w_g \quad h_g\right) \tag{3a}$$

$$\mathrm{Re}_2 = \frac{G_2}{\pi\mu d_p} \tag{3b}$$

Where $C_{s,2}$ and Re_1 are the conductance and the Reynolds number related to the air mass flow rate G_2. P_2 is the absolute pressure downstream of the supply holes of the pad and it is related to the mean air gap pressure through a semi-empirical formulation (Eq. 4).

$$P_0 = \left[1 - a_f^{\left(\frac{b_f}{h_{\mu m}}\right)}\right] \quad (P_2 - P_a) + P_a \tag{4}$$

Where, P_a is the ambient pressure, $h_{\mu m}$ is the value of the air gap height expressed in μm, $a_f = 0.02$ and $b_f = 5$ μm are experimental coefficients that depends on the type of air pad that is considered. Once in the clearance, the flow air divided in two sub-flows G_{fb} and G_3. The first one (G_{fb}) travels towards the volume V_{fb} of the chamber 2 of the valve (whose pressure is designated by P_{fb}), while the second one (G_3) is exhausted into atmosphere. The expression of the feedback flow G_{fb} is similar to those of G_1 and G_2 (see Eq. 5).

$$G_{fb} = K_T C_{s,fb} P_0 \sqrt{1 - \left(\frac{\frac{P_{fb}}{P_0} - b_c}{1 - b_c}\right)^2} \tag{5}$$

$$C_{s,fb} = 1.05\left(1 - 0.3e^{-0.005\mathrm{Re}_{fb}}\right) \quad \frac{0.685}{\sqrt{R_g\ T}} \quad \pi \quad d_{fb} \quad h \tag{5a}$$

$$\mathrm{Re}_{fb} = \frac{G_{fb}}{\pi\mu d_{fb}} \tag{5b}$$

Where $C_{s,fb}$ and Re_{fb} are the conductance and the Reynolds number related to the air mass flow rate G_{fb} passing through the pressure intake. G_3 is computed as the sum of the outflows from the edges of the pad along x and y directions (see Eq. 6).

$$G_3 = 2\left(G_x + G_y\right) = \frac{h^3\left(P_0^2 - P_a^2\right)}{6\mu R_g T}\left(\frac{b}{L-l} + \frac{l}{B-b}\right) \tag{6}$$

$$G_x = \frac{h^3\left(P_0^2 - P_a^2\right)}{12\mu R_g T}\frac{b}{L-l} \tag{6a}$$

$$G_y = \frac{h^3\left(P_0^2 - P_a^2\right)}{12\mu R_g T}\frac{l}{B-b} \tag{6b}$$

The force produced by the fluid pressure is computed by considering a constant pressure distribution within the surface enclosed by the grooves (of dimensions l and b) and a linear one outside this region (see Fig. 4). By summing up the contributions in these two regions it is possible to obtain the expression of Eq. 7.

$$F_p = \frac{(P_0 - P_a)}{3}\left[lb + LB + \frac{(Lb + lB)}{2}\right] \tag{7}$$

The equilibrium position of the system is computed considering the force balance equation of Eq. 8.

$$M\ddot{h} = F_{ext} - F_p \tag{8}$$

Where, F_{ext} is the external force applied to the pad and M is the moving mass supported by the pad. The other state equations of the model are related to the continuity equation applied to the pad chamber (Eq. 9), the feedback chamber (Eq. 10) and the air gap volume V_2 (Eq. 11).

$$G_1 - 4G_2 = \frac{V_1}{R_g T}\frac{dP_1}{dt} \tag{9}$$

$$4G_2 - G_3 - G_{fb} = \frac{V_2}{RT}\frac{dP_0}{dt} + \frac{P_0 lb}{RT}\frac{dh}{dt} \tag{10}$$

$$V_2 = V_0 + V_g = lbh + 2w_g h_g(l+b) \tag{10 a}$$

$$G_{fb} = \frac{V_{fb}}{RT}\frac{dP_{fb}}{dt} + \frac{A_{fb}P_{fb}}{RT}\frac{dx}{dt} \tag{11}$$

$$A_{fb} = \frac{\pi}{12}\left[d_M^2 - d_m^2 + d_o(d_M - d_m)\right] \tag{11a}$$

$$V_{fb} = V_{fb_0} + A_{fb}x \tag{11b}$$

Where, A_{fb} is an equivalent area that corresponds to the variation of the volume V_{fb} when the shutter moves downwards or upwards. V_{fb_0} is the volume of the feedback chamber when the rubber membranes suspending the shutter are undeformed.

3.2. Simplified model

Fig. 9 shows the pneumatic scheme of the simplified model.

Unlike the complete model, the simplified model presents only three state equations: the force balance equation of the pad (8), the continuity equation applied to its internal chamber (9) and air gap volume (10). This choice was made since it significantly reduces the time-cost of numerical simulations and it is reasonable to assume that the dynamics of the shutter and feedback chamber filling should not have much influence on the static characteristics of the system. In view of this, the main goal of using a simplified model is to compare its accuracy and time-cost with respect to the complete model.

3.3. Numerical algorithm

The lumped model of the system is implemented in Matlab using the finite difference method and integrating the state equation through the forward Euler scheme. Due to their nonlinear nature, the state equations are solved simulating the system behaviour over the time assuming a time step (Δt) of 10^{-7} and 5 10^{-6} s for the complete and simplified model respectively. Since the compensating action of the valve renders the load capacity F_p and the air mass flow rate G non-injective functions of the air gap height h (there are more than one load capacities and air mass flow rates for the same air gap height value), the equilibrium of the system must be computed using the external force F_{ext} as input for the model [38]. However, both the numerical models require as input suitable initial conditions (P_{1_0}, P_{0_0}, P_{fb_0}, h_0, $\dot{h}_0$, x_{0_0}, $\dot{x}_0$ for the complete model and P_{1_0}, P_{0_0}, h_0, $\dot{h}_0$ for the simplified one) to efficiently solve this initial value problem. These initial values of the complete model were computed by imposing an initial and constant ($\dot{h}_0$=0) air gap height h_0 and solving Eqs. 2, 9, 10 and 11 for x_{0_0}, $\dot{x}_0$, P_{1_0}, P_{0_0}, P_{fb_0}.

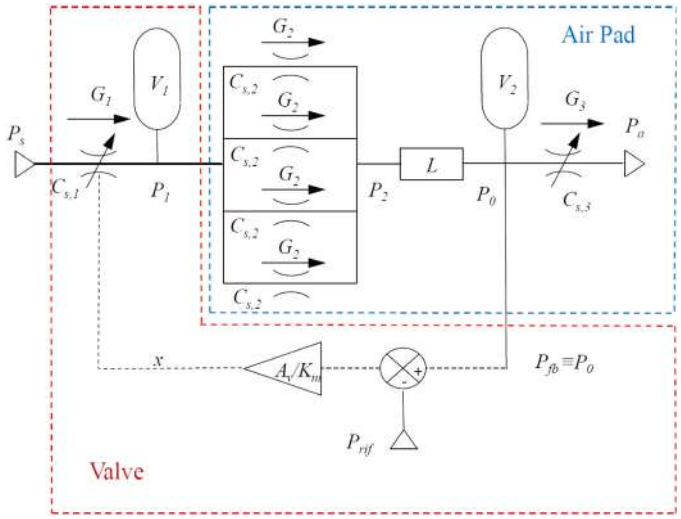

Fig. 9. Pneumatic scheme of the simplified model.

The same procedure was used for the simplified model. At this point, the values of the state variable at the equilibrium were computed imposing the external force F_{ext} and iteratively solving the equation till the converge is reached. The convergence of the algorithm was evaluated considering the following conditions:

$$\frac{h^{t+1} - h^t}{h^t} < \varepsilon_h$$

$$\frac{F_p^{t+1} - F_p^t}{F_p^t} < \varepsilon_F$$

where, h^t and F_p^t air the air gap height and the load capacity of the gap compute at t^{th} iteration. ε_h and ε_F are the selected tolerance that was chosen equal to 10^{-7}.

4. Results and discussions

The obtained experimental and numerical results were obtained under different values of the supply (P_s) and reference (P_{rif}) pressures to investigate the prototype performances. The values of the supply pressure P_s were 0.4, 0.5 and 0.6 absolute MPa, while 0,1, 0.2, 0.225, 0.25, 0.275 absolute MPa were chosen as reference pressure values. This section discusses and compares experimental and numerical results. The first part (Section 4.1) shows the experimental results by explaining the connections between the shapes of the experimental curves and the working principle of the system. The aim of the second part (Section 4.2) is to compare experimental and numerical results to validate the model. The last part (Section 4.3) compares the results obtained from the complete and simplified models to evaluate their pros and cons.

4.1. Experimental results

4.1.1. Supply pressure effect

Figs. 10, 11, 12 and 13 show results from the experimental static characterisation of the proposed prototypes. The results reported in Figs. 10 and 11 are related to the load capacity and the air consumption of the pad in the presence of a constant reference pressure P_{rif}= 0.1 absolute MPa and different supply pressures P_s= 0.4, 0.5, 0.6 absolute MPa.

In this case, the system exhibits static curves that are similar to those obtained in the absence of the differential diaphragm valve, i.e., the system does not compensate for load variations. In fact, it can be seen that the load capacity and air consumption curves are characterised by nonlinear trends that are almost proportional with respect to the supply pressure P_s. When the air gap reduces the load capacity increases due to the increase of the mean air gap pressure, while the air consumption reduces since the air gap conductance reduces too.

Conversely, as the reference pressure P_{rif} increases, the contribution of the regulating action of the valve becomes more evident. This can be seen in Figs. 12 and 13. Here, where the reference pressure was P_{rif}= 0.2 absolute MPa, the regulating action of the valve is relevant and modifies the trends of the static curves. Here, it is possible to distinguish three different behaviours that can be explained on the basis of the working principle described through Fig. 4 in Section 2.1. Starting from higher air gap heights, a by-pass, a regulation and a saturation zone can be identified. The by-pass region extends up to point A_i. The subscripts 4, 5 and 6 are related to the values of the supply pressure imposed during the tests and expressed in bar. Here, the valve behaves like a linear pneumatic resistance, since the value of the feedback pressure P_{fb} (see Fig. 4) is not sufficient to create a well-defined gap between the nozzle and the shutter. Consequently, the air consumption of the system is due to small air leakages occurring because the shutter cannot perform of a perfect closure of the valve nozzle. When the external load increases, the nozzle-shutter distance increases because of the higher feedback pressure $P_{fb}$and the valve starts regulating (after point A_i). During the regulation,

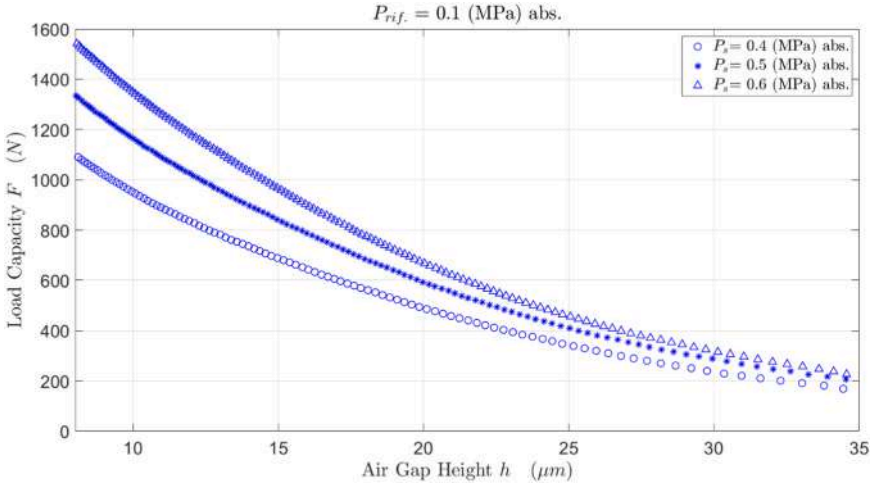

Fig. 10. Experimental load capacity at $P_{rif.}$= 0.1 absolute MPa and different supply pressures P_S= 0.4, 0.5, 0.6 absolute MPa.

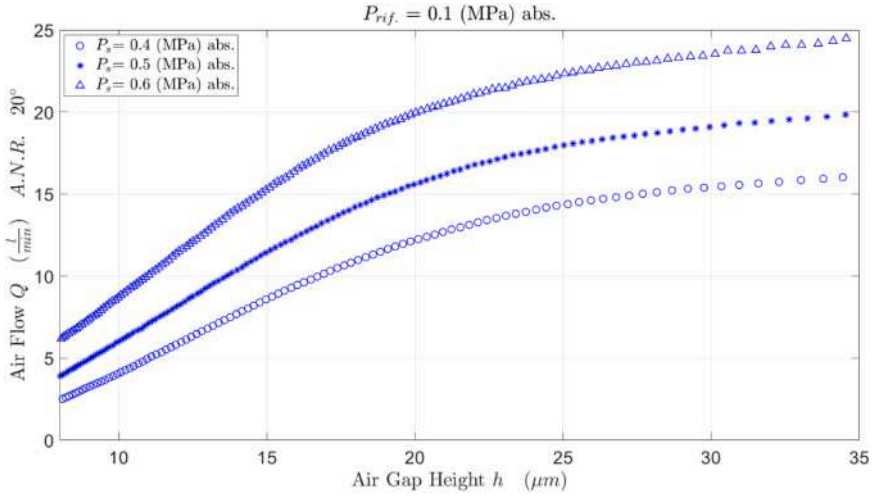

Fig. 11. Experimental air consumption at $P_{rif.}$= 0.1 absolute MPa and different supply pressures P_S= 0.4, 0.5, 0.6 absolute MPa.

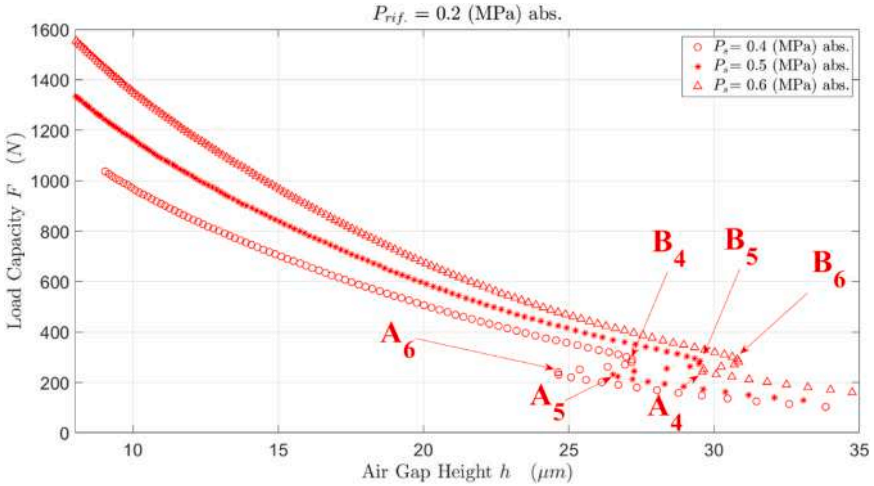

Fig. 12. Experimental load capacity at $P_{rif.}$= 0.2 absolute MPa and different supply pressures P_S= 0.4, 0.5, 0.6 absolute MPa.

the valve compensates for the air gap variation by increasing the air flow rate supplied to the pad. The valve regulation ends at point B_i when the nozzle saturates because of its excessive distance from the shutter. This operating condition corresponds to the maximum air consumption of the system (see Fig. 13). In the saturation zone (after point B_i), the load and air consumption curves exhibit the same trends of Figs. 10 and 11, i.e.

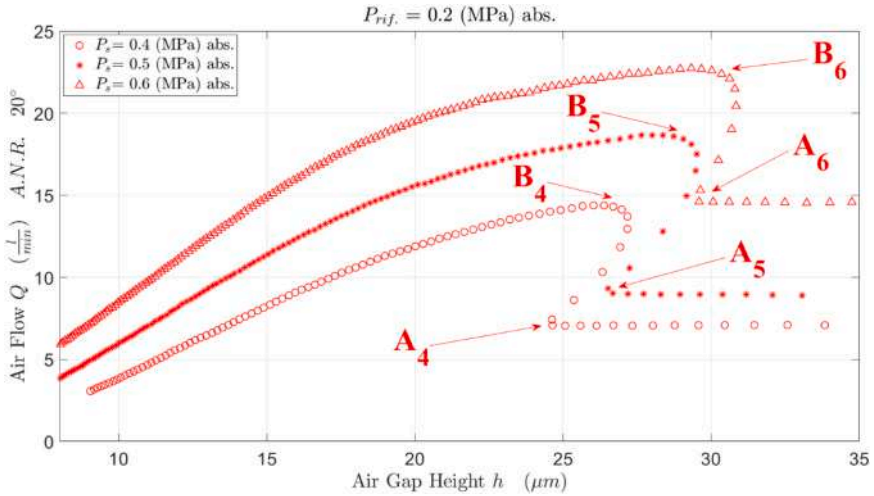

Fig. 13. Experimental air consumption at $P_{rif.}$= 0.2 absolute MPa and different supply pressures P_S= 0.4, 0.5, 0.6 absolute MPa.

those of a convention pad.

Additionally, also in the cases of Figs. 12 and 13, the static curves are almost proportional to the supply pressure P_s.

4.1.2. Reference pressure effect

Figs. 14 and 15 show the experimental results obtained in the presence of a constant supply pressure P_s= 0.4 absolute MPa and different reference pressures P_{rif}= 0.1, 0.2, 0.225, 0.25, 0.275 absolute MPa. Here, the regulation zones correspond to the part of curve between A_i and B_i. it can be seen that the extension of the regulation and saturation zones gradually reduces as the reference pressure is increased. Conversely, the portion of the by-pass region increases with the reference pressure.

During some tests, a poor repeatability was observed. This was probably caused by the rubber membranes used to guide the shutter during its linear motion: the motion of the shutter does not follow the same trajectory every time. This can be seen analysing the trend of the air consumption curves in the by-pass region (see Figs. 15, 17 and 19). Here, it is possible to see that, at the same supply pressure, the air consumption is almost constant, but it is not the same when the reference pressure is changed. Figures from 16–19 show the experimental results obtained similar to those shown in Figs. 14 and 15 but in the presence of supply pressures of 0.5 and 0.6 absolute MPa.

4.2. Model validation

Figs. 20 and 21 compares the numerical and experimental results obtained in the presence of a constant supply pressure of 0.4 absolute MPa and different reference pressures P_{rif}= 0.1, 0.2, 0.225, 0.25, 0.275 absolute MPa.

In particular, the numerical results are obtained through the simplified version of the implemented lumped parameters model. The comparisons that are shown in Fig. 20 demonstrate that the model is quite accurate since the results provided by the model are globally in good agreement with the experimental ones.

4.3. Numerical comparison

Figs. 22 and 23 compares the load capacity and air consumption curves obtained at P_S= 0.4 absolute MPa and different reference pressures P_{rif}= 0.1, 0.2, 0.225, 0.25, 0.275 absolute MPa through the complete and simplified versions of the proposed lumped parameter model. As can be seen, these two models provide almost identical results regarding load capacity and air consumptions.

The implications of this perfect agreement are quite relevant since the use of the simplified model makes it possible to significantly reduce the time effort of the numerical simulations. Indeed, the simplified model solves less equations and exhibits a higher numerical stability. This makes it possible to use a larger time step (5 10^{-6} against 1 10^{-7}).

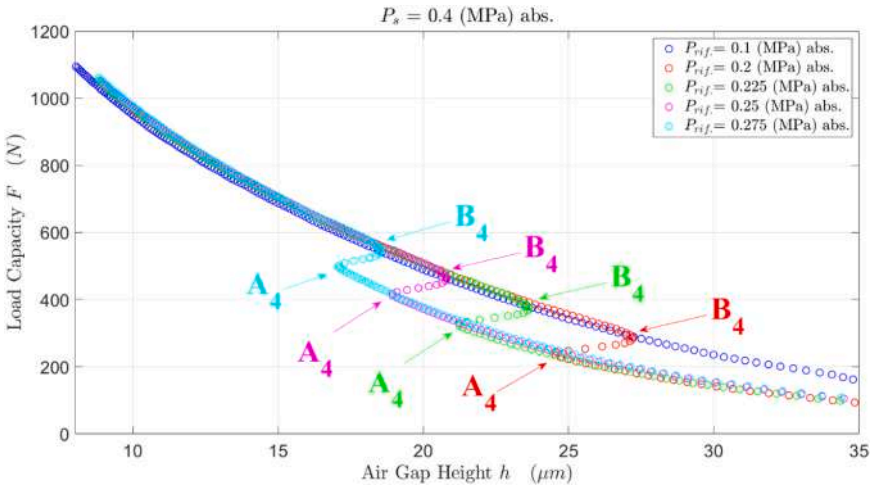

Fig. 14. Experimental load capacity at P_S= 0.4 absolute MPa and different reference pressures P_{rif}= 0.1, 0.2, 0.225, 0.25, 0.275 absolute MPa.

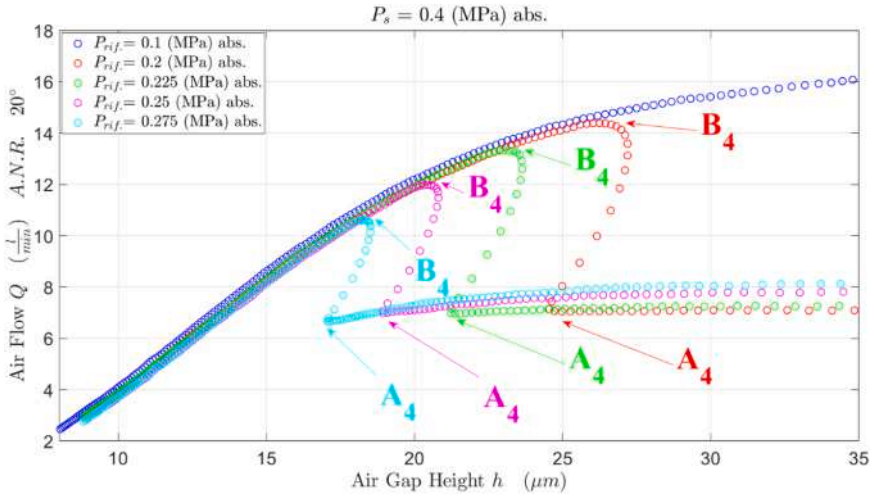

Fig. 15. Experimental air consumption at P_S= 0.4 absolute MPa and different reference pressures P_{rif}= 0.1, 0.2, 0.225, 0.25, 0.275 absolute MPa.

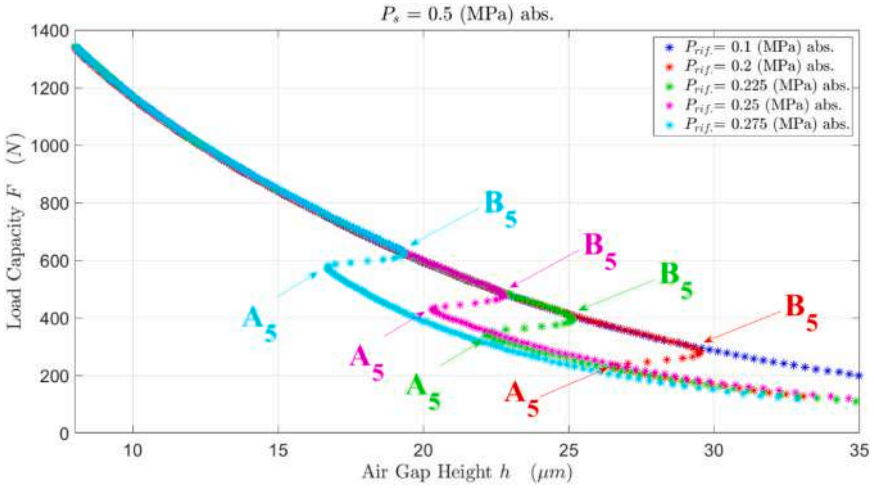

Fig. 16. Experimental load capacity at P_S= 0.5 absolute MPa and different reference pressures P_{rif}= 0.1, 0.2, 0.225, 0.25, 0.275 absolute MPa.

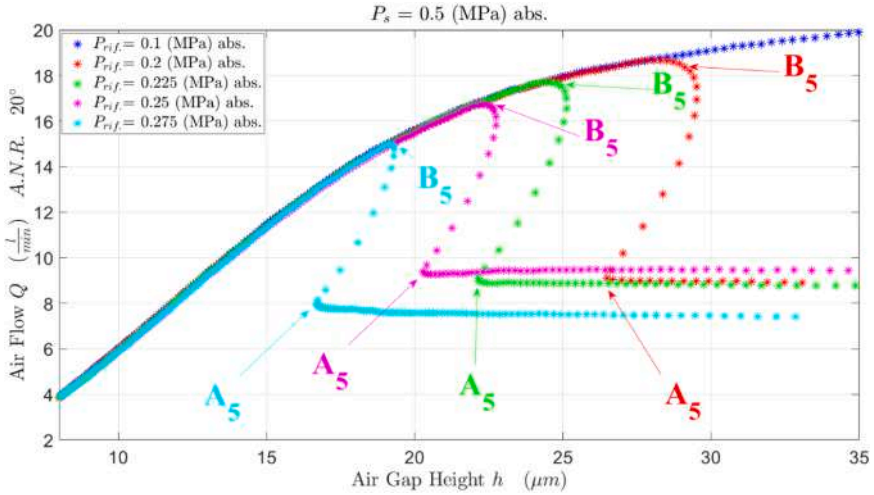

Fig. 17. Experimental air consumption at P_S= 0.5 absolute MPa and different reference pressures P_{rif}= 0.1, 0.2, 0.225, 0.25, 0.275 absolute MPa.

Table 1 compares the simulation time of three different simulations.

The static curves obtained in these simulations were computed starting from an initial air gap of 4 μm corresponding to maximum load capacity and reducing step by step the external force applied upon the pad of 30 N for each equilibrium point till reaching a minimum load capacity of 150 N.

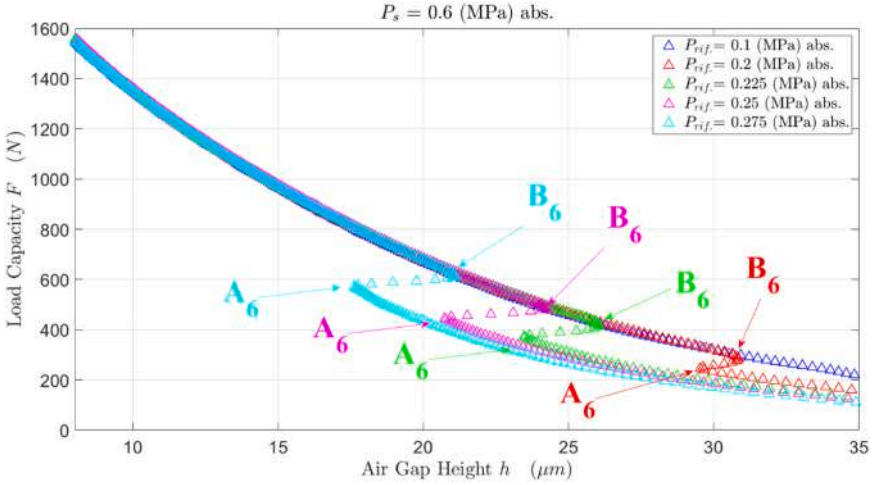

Fig. 18. Experimental load capacity at P_S= 0.6 absolute MPa and different reference pressures P_{rif}= 0.1, 0.2, 0.225, 0.25, 0.275 absolute MPa.

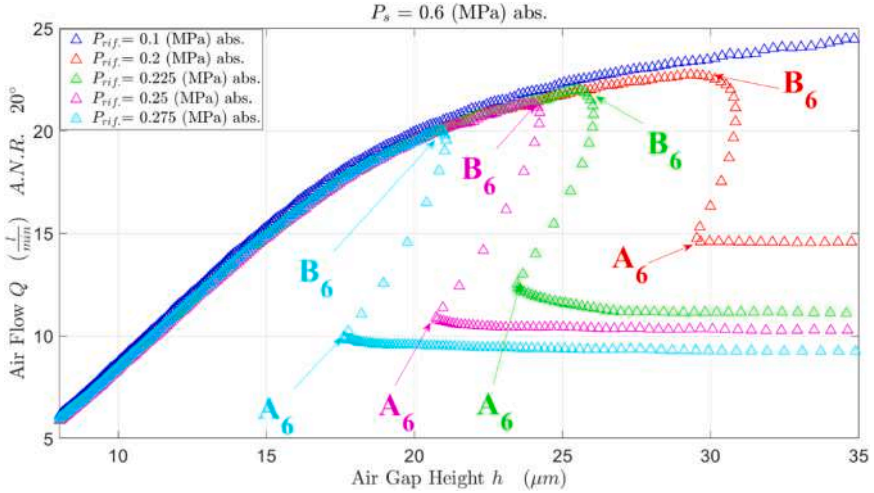

Fig. 19. Experimental air consumption at P_S= 0.5 absolute MPa and different reference pressures P_{rif}= 0.1, 0.2, 0.225, 0.25, 0.275 absolute MPa.

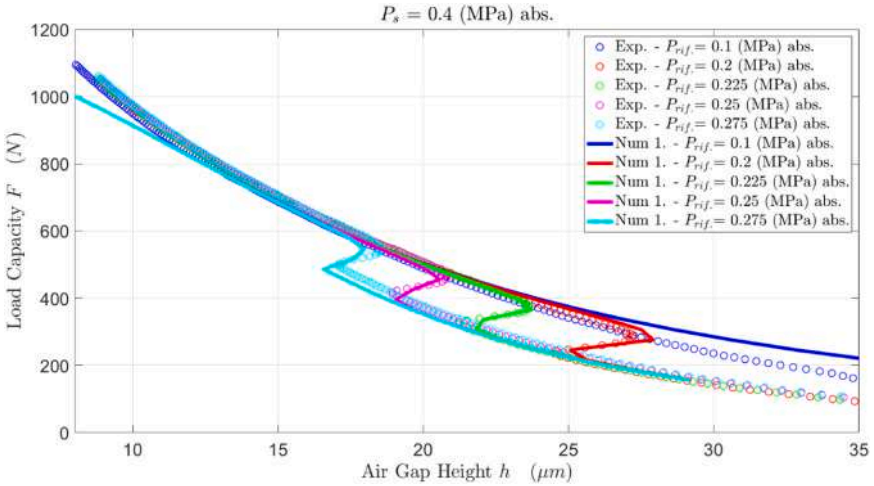

Fig. 20. Comparison between the experimental and numerical load capacity curves obtained at P_S= 0.4 absolute MPa and different reference pressures P_{rif}= 0.1, 0.2, 0.225, 0.25, 0.275 absolute MPa.

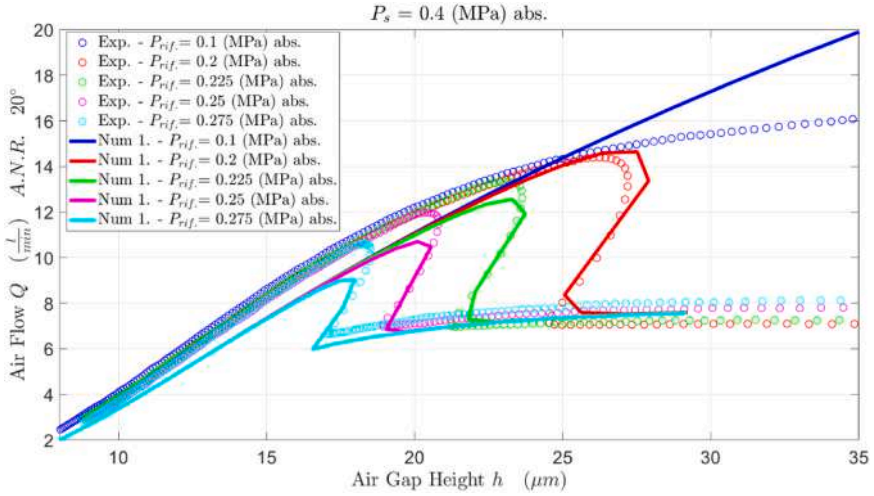

Fig. 21. Comparison between the experimental and numerical air consumption curves obtained at P_S= 0.4 absolute MPa and different reference pressures P_{rif}= 0.1, 0.2, 0.225, 0.25, 0.275 absolute MPa.

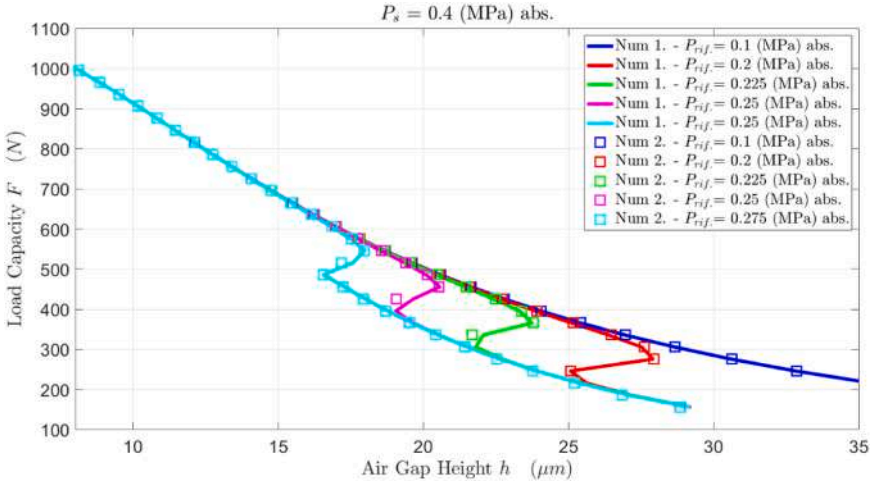

Fig. 22. Comparison between the experimental and numerical load capacity curves obtained through the complete and simplified lumped parameter models at P_S= 0.4 absolute MPa and different reference pressures P_{rif}= 0.1, 0.2, 0.225, 0.25, 0.275 absolute MPa.

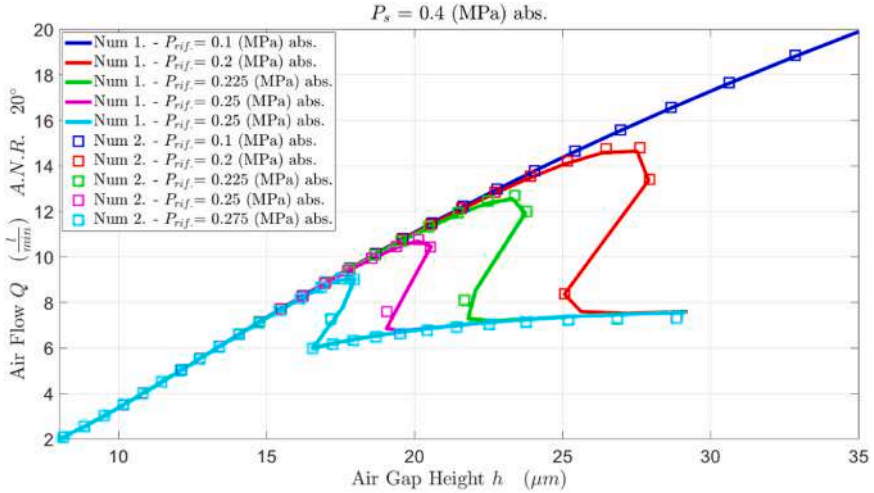

Fig. 23. Comparison between the numerical air consumption curves obtained through the complete and simplified lumped parameter models at P_S= 0.4 absolute MPa and different reference pressures P_{rif}= 0.1, 0.2, 0.225, 0.25, 0.275 absolute MPa.

Table 1
Comparison between the simulation time of the complete and simplified model.

Test	Complete Model Simulation time (s)	Simplified Model Simulation time (s)
P_s= 0.4 MPa, P_{rif}= 0.275 MPa	85.12	1.109
P_s= 0.5 MPa, P_{rif}= 0.275 MPa	103.0	3.233
P_s= 0.6 MPa, P_{rif}= 0.275 MPa	159.4	3.286

In view of this, the static curves computed with higher supply pressures presents more equilibrium points and thus a higher computational time. Comparing the computational effort of the model it is possible to see that the simplified version is about fifty time faster than the complete one.

5. Conclusions

This paper presented a novel prototypes of passively compensated air pad. The system consists in the integration of a conventional pad and a differential diaphragm valve. This kind of valve was designed in an attempt to increase the accuracy of the valve regulation. The main differences with respect to previous solutions are that the valves present four chambers and the inflow provided to the pad depends on the relative position between a fixed nozzle and a moving shutter. The motion of the shutter is defined by the values of a feedback pressure taken from the air gap, whereas its initial position is defined by a reference pressure that can be suitably chosen by external users. The functioning and performance of the proposed prototype were verified by means of a suitable experimental set-up. The load capacity and air consumption curves of the system were measured in the presence of different supply (P_s=0.4, 0.5, 0.6 absolute MPa) and reference pressures (P_{rif}=0.1, 0.2, 0.225, 0.25, 0.275 absolute MPa). Experimental results confirm the effectiveness of the proposed compensation solution demonstrating that the system exhibits quasi static infinite stiffness over a small portion of its static characteristics. Despite the higher complexity of the valve structure, the accuracy of regulation is comparable to that of previous solutions [38]. Moreover, as in the previous solutions, the stiffness of the system can be optimized only through a suitable design procedure [37] that makes it possible to compute the optimal parameters of the valve, i.e., reference pressure, membrane stiffness and nozzle diameter. Indeed, in this case, due to the absence of such procedure, the prototype exhibit overcompensation, i.e., the valve provides the pad with an air flow higher than that required to keep constant the air gap height when the applied force is increased.

The system was modelled through two lumped parameter models consisting in a series of pneumatic resistances and capacitances. These two models are characterised by a different level of complexity to compare their computational costs and they were implemented in Matlab, discretized by the finite difference method according to forward Euler integration scheme. The experimental results closely aligned with the numerical simulations, particularly in terms of load capacity. The comparison between the complete and simplified version of the model demonstrates that the models provided almost the same static curves. By contrast, the simulation time of the simplified version of the model is about fifty times less than that of the complete version. These results suggest that the proposed method holds promise as an efficient and cost-effective approach for improving the static performance of aerostatic pads.

Statement of originality

I am here with confirm that paper titled “An Aerostatic Pad Compensated by a Differential Diaphragm Valve” submitted for consideration for the publication in the journal “Tribology International” is an original study done by the authors. To the best knowledge of authors, the study in the present article has not been published earlier in any journal by the authors or anybody else.

Declaration of Competing Interest

The authors declare that they have no known competing financial interests or personal relationships that could have appeared to influence the work reported in this paper.

Data Availability

Data will be made available on request.

References

[1] Fetting C. The European green deal. ESDN Report 2020;53.
[2] Chen G, Ju B, Fang H, Chen Y, Yu N, Wan Y. Air bearing: academic insights and trend analysis. Int J Adv Manuf Technol 2020;106:1191–202.
[3] Zhao Q, Qiang M, Hou Y, Chen S, Lai T. Research developments of aerostatic thrust bearings: a review. Appl Sci 2022;12:11887. https://doi.org/10.3390/app122311887.
[4] Gao Q, Chen W, Lu L, Huo D, Cheng K. Aerostatic bearings design and analysis with the application to precision engineering: state-of-the-art and future perspectives. Tribology Int 2019;135:1–17.
[5] Lentini L, Moradi M, Colombo F. A historical review of gas lubrication: from reynolds to active compensations. Tribology Ind 2018;40:165–82. https://doi.org/10.24874/ti.2018.40.02.01.
[6] Wen Z, Gu H, Shi Z. Key technologies and design methods of ultra-precision aerostatic bearings. Lubricants 2023;11:315.
[7] Powell JW. Design of aerostatic bearings. Machinery Publishing,; 1970.
[8] Rowe WB. Hydrostatic. Aerostatic, and Hybrid Bearing Design. Elsevier,; 2012.
[9] Boffey DA, Duncan AE, Dearden JK. An experimental investigation of the effect of orifice restrictor size on the stiffness of an industrial air lubricated thrust bearing. Tribology Int 1981;14:287–91.
[10] Colombo F, Lentini L, Raparelli T, Trivella A, Viktorov V. Dynamic characterisation of rectangular aerostatic pads with multiple inherent orifices. Tribology Lett 2018;66. https://doi.org/10.1007/s11249-018-1087-x.
[11] Yu P, Lu J, Luo Q, Li G, Yin X. Optimization design of aerostatic bearings with square micro-hole arrayed restrictor for the improvement of stability: theoretical predictions and experimental measurements. Lubricants 2022;10:295.
[12] Chang SH, Chan CW, Jeng Y-R. Discharge coefficients in aerostatic bearings with inherent orifice-type restrictors. J Tribology 2015;137.
[13] Chen X, Chen H, Luo X, Ye Y, Hu Y, Xu J. Air vortices and nano-vibration of aerostatic bearings. Tribology Lett 2011;42:179–83.
[14] Al-Bender F. On the modelling of the dynamic characteristics of aerostatic bearing films: From stability analysis to active compensation. Precis Eng 2009;33:117–26. https://doi.org/10.1016/j.precisioneng.2008.06.003.
[15] Al-Bender F. Air Bearings: Theory, Design and Applications. John Wiley & Sons; 2021.
[16] Raparelli T, Viktorov V, Colombo F, Lentini L. Aerostatic thrust bearings active compensation: critical review. Precis Eng 2016;44:1–12.
[17] Colombo F, Lentini L, Raparelli T, Viktorov V. Actively compensated aerostatic thrust bearing: design, modelling and experimental validation. Meccanica 2017:1–16. https://doi.org/10.1007/s11012-017-0689-y.
[18] Maamari N, Krebs A, Weikert S, Wild H, Wegener K. Stability and dynamics of an orifice based aerostatic bearing with a compliant back plate. Tribology Int 2019;138:279–96.
[19] Maamari N, Krebs A, Weikert S, Wegener K. Centrally fed orifice based active aerostatic bearing with quasi-infinite static stiffness and high servo compliance. Tribology Int 2019;129:297–313.
[20] Aguirre G, Al-Bender F, Van Brussel H. A multiphysics model for optimizing the design of active aerostatic thrust bearings. Precis Eng 2010;34:507–15. https://doi.org/10.1016/j.precisioneng.2010.01.004.
[21] Luo X, Han B, Chen X, Li X, Jiang W. Multi-physics modeling of tunable aerostatic bearing with air gap shape compensation. Tribology Int 2021;153:106587.
[22] Colombo F, Maffiodo D, Raparelli T. Active gas thrust bearing with embedded digital valves and backpressure sensors. Tribology Trans 2017;60:807–13. https://doi.org/10.1080/10402004.2016.1213344.
[23] Morosi S, Santos IF. Active lubrication applied to radial gas journal bearings. Part 1: modeling. Tribology Int 2011;44:1949–58. https://doi.org/10.1016/j.triboint.2011.08.007.
[24] Pierart FG, Santos IF. Active lubrication applied to radial gas journal bearings. Part 2: Modelling improvement and experimental validation (Complete) Tribology Int 2016:237–46. https://doi.org/10.1016/j.triboint.2015.12.004.
[25] Blondeel E., Snoeys R., Devrieze L. Externally pressurized bearings with variable gap geometries. 7th International Gas Bearing Symposium, vol. 2, Southampton: 1976.
[26] Blondeel E, Snoeys R, Devrieze L. Dynamic stability of externally pressurized gas bearings. J Lubr Technol 1980;102:511–9.

[27] Snoeys R, Al-Bender F. Development of improved externally pressurized gas bearings. KSME J 1987;1:81–8. https://doi.org/10.1007/BF02953383.
[28] Holster PL, Jacobs JAH. Theoretical analysis and experimental verification on the static properties of externally pressurized air-bearing pads with load compensation. Tribology Int 1987;20:276–89. https://doi.org/10.1016/0301-679X(87)90028-4.
[29] Bryant M.R., Velinsky S.A., Beachley N.H., Fronczak F.J. A Design Methodology for Obtaining Infinite Stiffness in an Aerostatic Thrust Bearing. Journal of Mechanisms, Transmissions, and Automation in Design 1986;108:448–453.
[30] Yoshimoto S, Anno Y, Hirakawa Y. Aerostatic thrust bearing with a self-controlled restrictor employing a floating disk: static characteristics. JSME Int J Ser C, Dyn, Control, Robot, Des Manuf 1994;37:369–75.
[31] Newgard PM, Kiang RL. Elastic orifices for pressurized gas bearings. A S L E Trans 1966;9:311–7. https://doi.org/10.1080/05698196608972147.
[32] Kodnyanko V, Shatokhin S, Kurzakov A, Pikalov Y. Mathematical modeling on statics and dynamics of aerostatic thrust bearing with external combined throttling and elastic orifice fluid flow regulation. Lubricants 2020;8:57.
[33] Kodnyanko V, Shatokhin S, Kurzakov A, Pikalov Y, Strok L, Pikalov I, et al. Theoretical efficiency study of output lubricant flow rate regulating principle on the example of a two-row aerostatic journal bearing with longitudinal microgrooves and a system of external combined throttling. Mathematics 2021;9:1698.
[34] Chen M-F, Lin Y-T. Dynamic analysis of the X-shaped groove aerostatic bearings with disk-spring compensator. JSME Int J Ser C 2002;45:492–501. https://doi.org/10.1299/jsmec.45.492.
[35] Chen MF, Huang WL, Chen YP. Design of the aerostatic linear guideway with a passive disk-spring compensator for PCB drilling machine. Tribology Int 2010;43:395–403. https://doi.org/10.1016/j.triboint.2009.07.001.
[36] Wu Y, Li C, Du J, Liu T, Zuo X. Pneumatic hammer characteristics of the aerostatic thrust bearing with central orifice and pressure-equalizing groove. Nonlinear Dyn 2023;111:2161–82.
[37] Colombo F, Lentini L, Raparelli T, Trivella A, Viktorov V. Design and analysis of an aerostatic pad controlled by a diaphragm valve. Lubricants 2021;9:47.
[38] Ghodsiyeh D, Colombo F, Lentini L, Raparelli T, Trivella A, Viktorov V. An infinite stiffness aerostatic pad with a diaphragm valve. Tribology Int 2020;141:105964.
[39] Colombo F, Lentini L, Raparelli T, Trivella A, Viktorov V. A nonlinear lumped parameter model of an externally pressurized rectangular grooved air pad bearing. Advances in Italian Mechanism Science, vol. 68. Springer; 2019. p. 490–7.
[40] Colombo F, Lentini L, Raparelli T, Trivella A, Viktorov V. A lumped model for grooved aerostatic pad. Advances in Service and Industrial Robotics, vol. 67. Springer International Publishing; 2019. p. 678–86.
[41] Belforte G, Raparelli T, Viktorov V, Trivella A. Discharge coefficients of orifice-type restrictor for aerostatic bearings. Tribology Int 2007;40:512–21. https://doi.org/10.1016/j.triboint.2006.05.003.
[42] Colombo F, Lentini L, Raparelli T, Trivella A, Viktorov V. An identification method for orifice-type restrictors based on the closed-form solution of reynolds equation. Lubricants 2021;9:55.